ARTICLES
https://doi.org/10.1038/s41561-021-00862-6

Dynamics of the abrupt change in Pacific Plate motion around 50 million years ago

Jiashun Hu [1,2] ✉, Michael Gurnis [1], Johann Rudi [3], Georg Stadler [4] and R. Dietmar Müller [5]

A drastic change in plate tectonics and mantle convection occurred around 50 Ma as exemplified by the prominent Hawaiian–Emperor Bend. Both an abrupt Pacific Plate motion change and a change in mantle plume dynamics have been proposed to account for the Hawaiian–Emperor Bend, but debates surround the relative contribution of the two mechanisms. Here we build kinematic plate reconstructions and high-resolution global dynamic models to quantify the amount of Pacific Plate motion change. We find Izanagi Plate subduction, followed by demise of the Izanagi–Pacific Ridge and Izu–Bonin–Mariana subduction initiation alone, is incapable of causing a sudden change in plate motion, challenging the conventional hypothesis on the mechanisms of Pacific Plate motion change. Instead, Palaeocene slab pull from Kronotsky intraoceanic subduction in the northern Pacific exerts a northward pull on the Pacific Plate, while its Eocene demise leads to a sudden 30–35° change in plate motion, accounting for about half of the Hawaiian–Emperor Bend. We suggest the Pacific Plate motion change and hotspot drift due to plume dynamics could have contributed nearly equally to the formation of the Hawaiian–Emperor Bend. Such a scenario is consistent with available constraints from global plate circuits, palaeomagnetic data and geodynamic models.

Two endmember hypotheses, an abrupt change in Pacific Plate motion[1,2] and a change in mantle plume dynamics[3–5], have been proposed to account for the Hawaiian–Emperor Bend (HEB). Assuming fixed Pacific hotspots, the Pacific Plate motion has been inferred to change its direction from more northerly before 47 Ma to west–northwest around 47 Ma, resulting in the distinctive bend in the Hawaiian–Emperor seamount chain[1,6]. Different plate circuits linking the Pacific to the Indo-Atlantic realm assuming fixed or moving hotspot reference frames also predict a variable but non-trivial change of Pacific Plate motion at the time of the HEB[7]. However, palaeomagnetic observations on the Emperor seamounts show that the hotspot source drifted southwards from about 80 to 50 Ma (refs. [3,8]). Despite drift of the Hawaiian hotspot, a substantial change in the absolute motion of the Pacific Plate is required at around 50 to 47 Ma to fit plate motion data[2,9,10]. The southward drift of the source of the Hawaiian hotspot is expected from global geodynamic models[4,5], but the magnitude and cause of the change in absolute motion of the Pacific Plate remain unresolved.

Several possibilities for explaining the change in Pacific Plate motion have emerged, including initiation of Izu–Bonin–Mariana (IBM) and Tonga–Kermadec subduction zones, which have been dated to about 50 Ma on the basis of analysis of recently acquired deep-sea drilling cores[11,12]. The idea is that new subduction zones on the western side of the Pacific would have pulled the Pacific Plate in their direction. Alternatively, when the spreading centre between the Izanagi and Pacific plates (Fig. 1a–c) putatively merged with the trench of the long-lasting subduction zone along the eastern margin of Asia from about 60 to 50 Ma, it could have triggered a chain reaction of tectonic events that led to plate reorganization[13]. The collision of India with Asia in the early Cenozoic era is approximately correlated in time with the change in plate motion, and this collision could have sparked Pacific Plate motion change[14], although it is not clear how a reduction in slab pull on the Indian Plate would lead to a change in the forces on the Pacific Plate. Simple geodynamic models have offered some guidance on the cause of plate motions but do not show a change in Pacific Plate motion with the collision of India with Asia[15]. Moreover, the models show that evolving mantle buoyancy in response to slow changes in subduction configurations lead only to slow changes in plate speed and direction since buoyancy forces require accumulation of slabs in the upper mantle[15]. With a plate reconstruction having the Izanagi Plate slowly merging with the east Asian margin[16], simple torque balances of the Pacific Plate suggest a change in forcing from northwards to westwards around 50 Ma[17], in support of the ridge-subduction hypothesis[13]. Nevertheless, previous work suggests that the mechanics of a sudden change in plate motion are more likely associated with changes in the nature of plate boundaries than with the slow accumulation of mantle buoyancy. Although subduction is the primary force on oceanic plates[18], the forces driving (from slab buoyancy) and resisting (from plate bending and interplate coupling) it are concentrated within subduction zones[19,20]. Realistically treating the forces on a plate as large as the Pacific requires a global domain, while capturing the shear zones between plates (where one plate slides by another), with the strength of plates and the nonlinearity of the mantle and lithosphere rheology (including plastic failure within the hinge zone) all accounted for, requires high resolution[21].

Numerical tests of conventional hypotheses

Although the fundamental physics of subduction in global models of plate motions remain a computational challenge, it can be captured[22]. In this article, we test the prevailing ideas of the change in Pacific Plate motion—Izanagi Ridge demise and IBM initiation. In addition, during the Cretaceous period, the southern part of the Pacific Plate saw the emplacement of large mantle plumes[23], and so we also explore whether that scenario could have changed the force balance. All three scenarios—ridge demise, IBM formation and

[1]Seismological Laboratory, California Institute of Technology, Pasadena, CA, USA. [2]Department of Earth and Space Sciences, Southern University of Science and Technology, Shenzhen, China. [3]Mathematics and Computer Science Division, Argonne National Laboratory, Lemont, IL, USA. [4]Courant Institute of Mathematical Sciences, New York University, New York, NY, USA. [5]School of Geosciences, The University of Sydney, Sydney, New South Wales, Australia. ✉e-mail: hujs@sustech.edu.cn

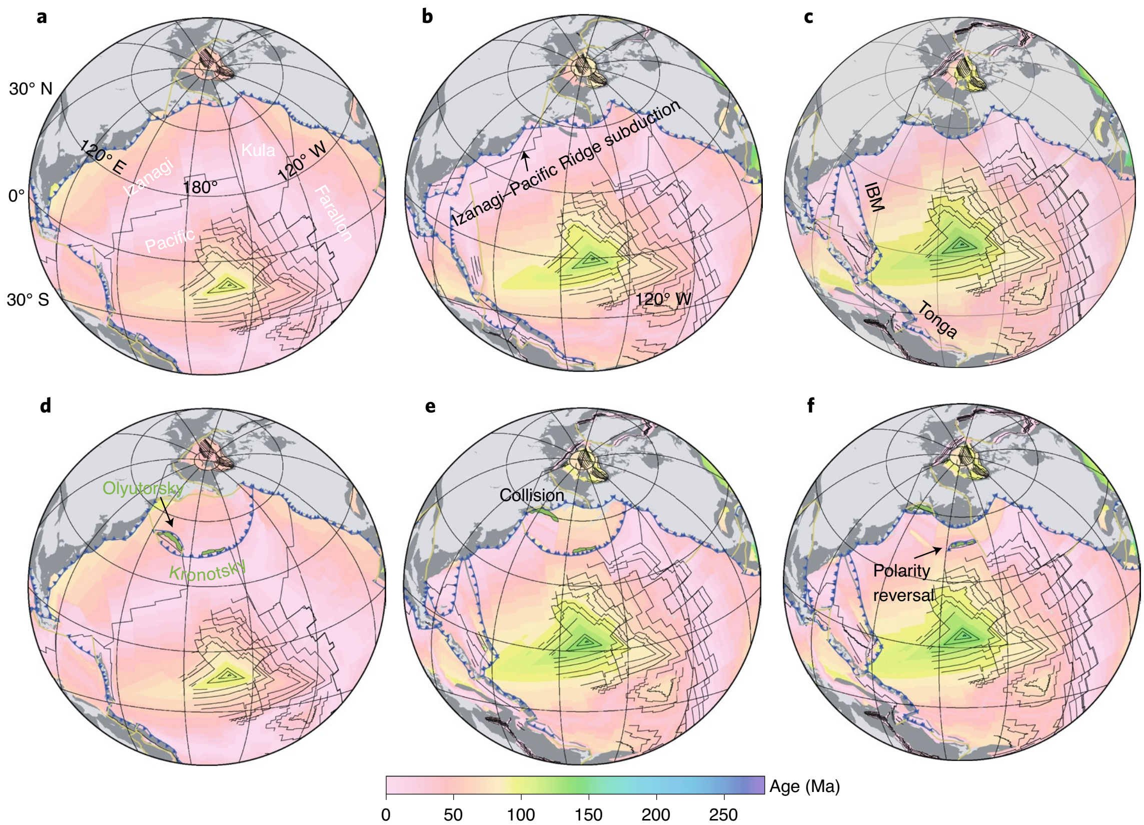

Fig. 1 | Alternative plate reconstruction models from Late Cretaceous to Eocene. a–c, The traditional plate reconstruction[9] that incorporates the subduction of the Izanagi--Pacific Ridge in the northern Pacific at 83 Ma (**a**), 60 Ma (**b**) and 47 Ma (**c**). **d–f**, The proposed plate reconstruction in this study that incorporates the Kronotsky intraoceanic subduction in the northern Pacific at 83 Ma (**d**), 50 Ma (**e**) and 47 Ma (**f**). Background colour indicates the seafloor age. Black lines in oceanic basins are the interpreted magnetic lineations from ref. [9]. The green terrains are the exotic Olyutorsky and Kronotsky arcs, respectively.

plume emplacement—fail to reproduce a sudden change in plate motion, leading to our development of an alternative reconstruction based on the exploration of proposed changes in intraoceanic subduction in the northern Pacific during the late Mesozoic era[24,25]. All these hypotheses, including the three scenarios and the alternative reconstruction, are cast as forward models by reconstructing thermal structures in the past through a combination of upper-mantle slabs generated with plate kinematics and lower-mantle slabs and mantle plumes, if appropriate, from spherical thermal convection models (Methods and Extended Data Figs. 1 and 2). The ancient plate and mantle thermal structures are then used in global dynamic models with realistic nonlinear rheologies[26] to predict plate deformations and motions (Fig. 2a). Key for the prediction of plate motions with realistic physics is the use of adaptive mesh refinement for the resolution of slab hinge zones and faults between plates (Fig. 2a,b).

On the basis of the reconstruction of the Pacific basin[9] with modifications (Methods and Fig. 1a–c) and incorporating Izanagi–Pacific Ridge subduction, we compute a set of models at 60, 50 and 47 Ma. The predicted velocities fit the reconstructed velocities well for most of the plates, especially at 47 Ma (Extended Data Fig. 3), validating the choice of rheological parameters (Methods). However, the models yield only a gradual change in Pacific Plate motion from 60 to 47 Ma with only a 10° change between 50 and 47 Ma (Fig. 3). The predicted Pacific Plate motion was oriented more westerly compared with that of the reconstruction at 50 Ma and earlier. Essentially, an extra force is needed either to pull or to push the Pacific Plate more towards the north before the change in plate motion. Neither the Izanagi–Pacific Ridge push that points mostly southwards (opposite the direction needed) nor the subsequent limited slab pull after the demise of the Izanagi–Pacific Ridge could provide such a force (Extended Data Fig. 3a,b). Keeping the plate margin configuration fixed, we attempted to find mantle models in which the Pacific Plate is pushed more to the north before 50 Ma. The emplacement of a large plume head below the southern Pacific Plate was associated with the eruption of the combined Ontong Java–Manihiki–Hikurangi plateaus at about 120 Ma (with a smaller pulse at about 90 Ma)[23]. The location of such positive buoyancy in the southern Pacific would seem to be well positioned to push the Pacific Plate to the north during the middle and late Cenozoic (Extended Data Fig. 4c). Although we may overestimate the plausible positive buoyancy associated with the event, the models fail to provide sufficient force to overcome the southward force of the Izanagi–Pacific spreading centre in the default reconstruction[9]. Compared with the standard model with Izanagi–Pacific Ridge subduction, the addition of this force causes only a small speed-up to the northwest (Extended Data Fig. 4e). Adding an even lower-viscosity shallow layer below the plate could lead to a further speed-up of the plate, but without changing the direction of plate motion (Extended Data Fig. 5).

Kronotsky intraoceanic subduction and Pacific Plate motion

With geological constraints from Kamchatka, we use an alternative reconstruction for the northern Pacific, which incorporates Kronotsky and Olyutorsky intraoceanic subduction (Fig. 1d–f). The

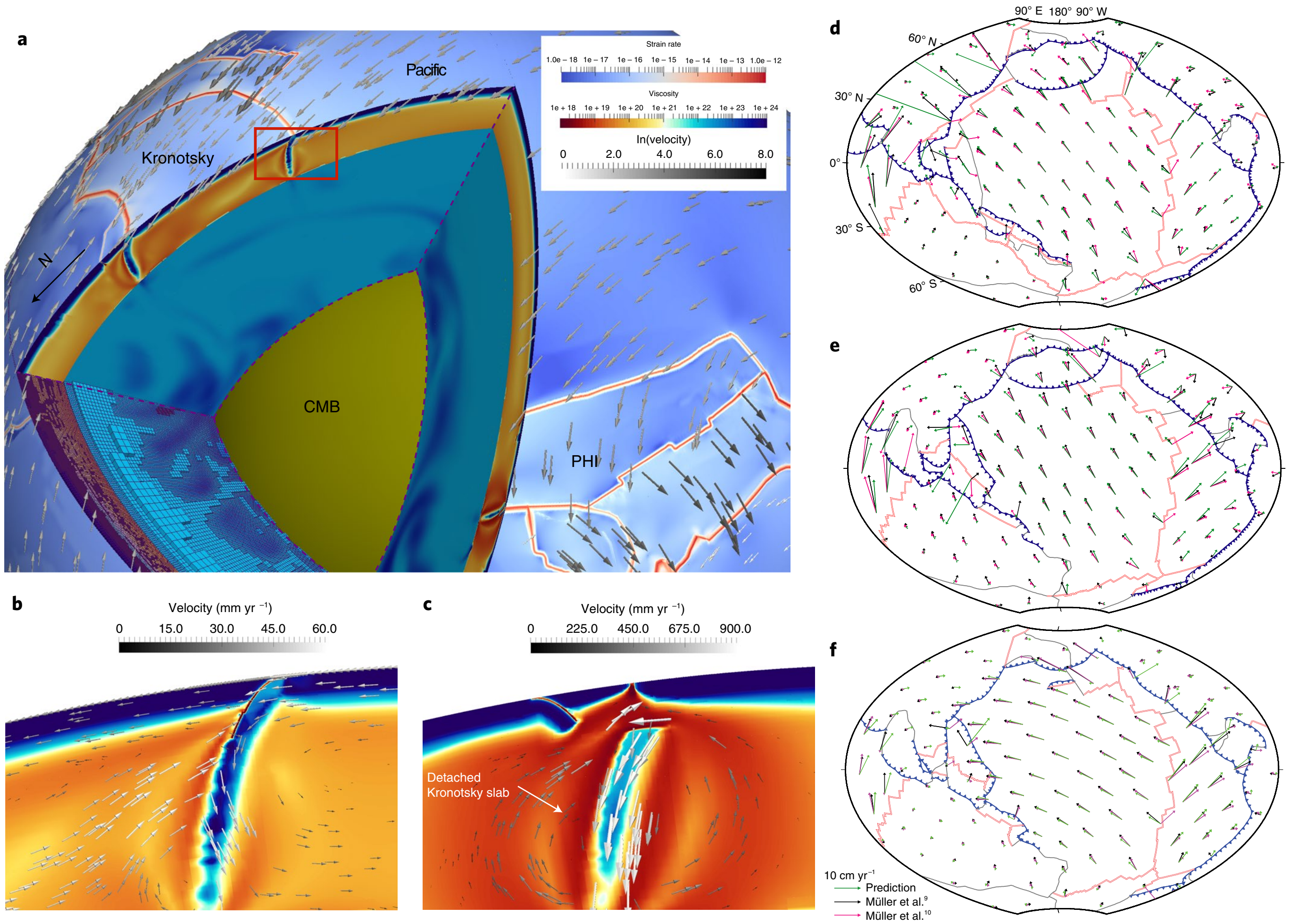

Fig. 2 | Geodynamic models used to predict plate motions. All models shown here are based on the proposed alternative reconstruction. **a**, Three-dimensional view of the geodynamic model at 50 Ma. **b**, Zoom into the Kronotsky subduction zone as indicated by the box in **a**. **c**, Cross section with the same location as in **b** but for the model at 47 Ma. **d–f**, Comparison of the geodynamically predicted plate motions with the geologically constrained plate motions taken from plate reconstructions at 60 Ma (**d**), 50 Ma (**e**) and 47 Ma (**f**). In **d**,**e**,**f**, the green arrows represent the velocities predicted by geodynamic models, the black arrows represent the velocities taken from the plate reconstruction of ref. [9] and the red arrows represent the velocities from ref. [10]. CMB, core-mantle boundary; PHI, Philippine Sea Plate.

associated Kronotsky and Olyutorsky arc complexes are now found in Kamchatka; but the palaeolatitudes of these arcs, as constrained by palaeomagnetic poles, show that both arcs are exotic, originating at mid-latitudes thousands of kilometres from their present-day locations[24]. The Kronotsky arc is interpreted to have been active from Late Cretaceous to Eocene and then accreted to the eastern margin of Kamchatka in late Miocene while the Olyutorsky arc originated at a similar age but accreted earlier, around 55–50 Ma (refs. [25,27]). The polarity of these arcs is uncertain, but their polarity must be consistent with plate tectonics and drift rates constrained by palaeomagnetic observations. Several studies have incorporated these arcs in regional reconstructions[28,29], showing that the Kronotsky arc corresponds to positive seismic velocity anomalies within the lower mantle. Before the Eocene, the Kronotsky subduction zone could have been responsible for a more northerly motion of the Pacific Plate. The subduction zone could have been much larger than considered here, but remnants within the Aleutians have not been found[28]. We have now incorporated the essence of these regional reconstructions by modifying a recent global model[9] (Fig. 1d–f). Essentially, in the reconstruction starting at 83 Ma, the Pacific Plate subducted below the Kronotsky arc, with the Olyutorsky arc forming a subduction zone with opposite polarity that rapidly migrated northwards away from the Kronotsky arc. In the reconstruction, we hypothesize that the Kronotsky subduction zone accommodated northward subduction of the Pacific Plate and that it seized up, triggering subduction polarity reversal with the Kronotsky arc rolling back to the north. This scenario is consistent with the placement of arcs and subduction zones inferred from the geology and palaeomagnetism of exotic terrains in Kamchatka[24] and is analogous to what occurred in the southwest Pacific during the Miocene, when the larger Melanesian subduction zone reversed polarity while segmenting into smaller arcs, such as New Britain and Vanuatu that then rolled back[30].

We built dynamic models based on this alternative reconstruction at 60, 50 and 47 Ma. The resultant plate motions provide better fits to kinematics, especially at 50 Ma (Fig. 2d–f) since the Kronotsky subduction zone provides an extra force to pull the Pacific Plate northwards (Fig. 2b). At 47 Ma, the demise of this force following the detachment of the slab during polarity reversal of the Kronotsky arc (Fig. 2c) causes the Pacific Plate motion to swing by ~30–35° to the west (Fig. 3). This provides a partial explanation for the abrupt change in Pacific Plate motion at 50 Ma. In contrast to the initiation of the IBM and Tonga–Kermadec subduction zones or the demise of the Izanagi–Pacific Ridge, the Kronotsky

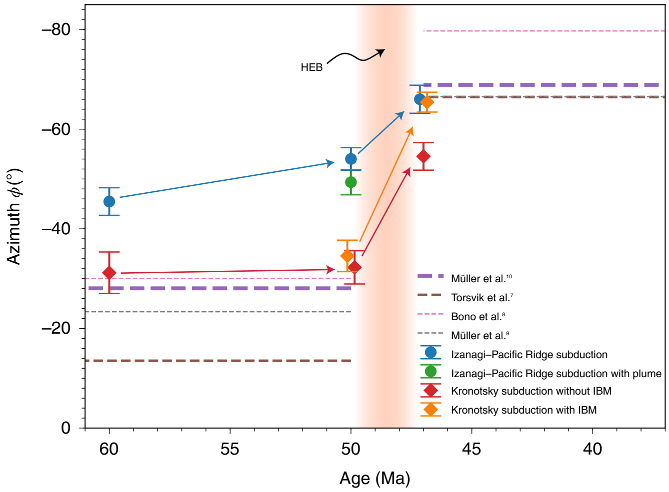

Fig. 3 | Change of the azimuth of the Pacific Plate motion with time. Symbols with filled colour represent the azimuths of the Pacific Plate motion from individual geodynamic models. The error bars represent the standard deviation of the azimuths in the region from 140° to 170° W longitude and from 10° to 35° N latitude on the Pacific Plate to accommodate the uncertainty of plume location. Dashed lines represent the average azimuths of the Pacific Plate motion before and after the HEB, calculated using different plate reconstruction models[7–10]. Before the HEB, the azimuth is averaged over the age range from 80 to 50 Ma; after the HEB, the azimuth is averaged over the range from 47 to 33 Ma.

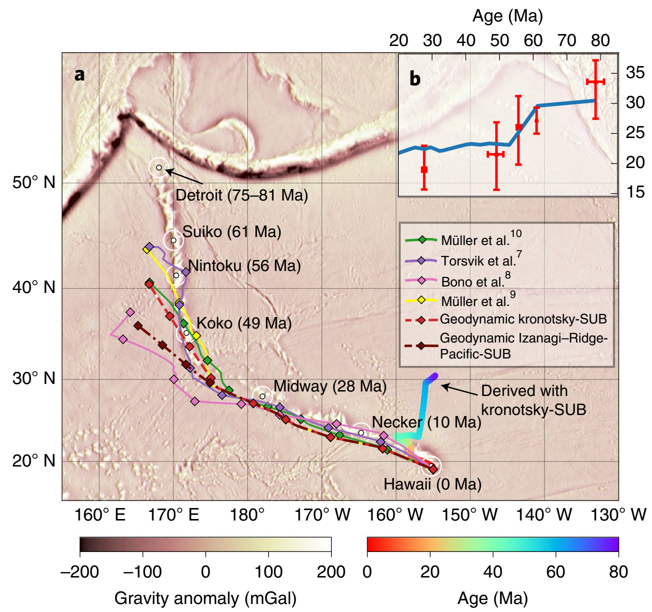

Fig. 4 | Computed tracks of the Pacific Plate motion and the residual hotspot drift. a, Tracks of the geodynamic models are computed using different plate reconstructions and geodynamic models. The tracks of the geodynamic models are computed using the Euler poles of Müller et al.[9] after 47 Ma and the interpolated motion based on two geodynamic models at 47, 50 and 60 Ma for the period from 80 to 47 Ma. Also shown is the first-order residual hotspot drift required to fit the age and the track of the Hawaiian-Emperor seamounts using our preferred Pacific Plate motion (labelled 'geodynamic Kronotsky-SUB'). **b**, Palaeolatitudes of the derived hotspot motion (thick blue line) and from palaeomagnetic data on Hawaiian-Emperor seamount samples (red error bars)[3].

subduction may have played a major role in causing an abrupt Pacific Plate motion change.

IBM subduction initiation and Pacific Plate motion

During IBM inception, a rapid (< 2 Myr duration) burst of forearc spreading over about 1,700 km along strike has been inferred from ages of basalts and boninites and might have been driven by the initial descent of the IBM slab[11]. This along-strike length is probably an overestimate at the time of initiation because of the spreading in the West Philippine Sea that occurred after 50 Ma (ref. [31]). The inferred spreading in the forearc would suggest a slab with a down-dip length of about 100 km after 2 Myr of subduction. At 50 Ma, we incorporated an IBM slab of mean down-dip length of 115 km, but over 3,000 km along strike, at least twice the probable length[11], considering the subduction could have initiated slightly earlier at 54 Ma (ref. [32]). Even by overestimating the negative buoyancy of the IBM slab, we find almost no change in direction of the Pacific Plate at 50 Ma compared with a model without this slab (Fig. 3 and Extended Data Fig. 6). Continued subduction to 47 Ma, however, now leads to a slab of up to 400 km in down-dip length and leads to a slab pull force to the west (Fig. 3 and Extended Data Fig. 7). Initiation of IBM subduction contributes about 10° of the change in plate motion out of the total 30–35° change associated with the demise of the Kronotsky. Also occurring at 50 Ma was the initiation of Tonga–Kermadec subduction. This initiation was associated with reverse faulting, folding and uplift over northern Zealandia and was probably driven by broad-scale compression induced by a change in plate motion[12]. Given substantial interplate coupling, it would be difficult to envision any additional force to pull the Pacific to the west from Tonga at 50 Ma.

Hawaiian hotspot drift

At about 50 Ma, there were abrupt changes in the southward velocity of the Hawaiian plume source[3] and in absolute Pacific Plate motion[2,9,10]. We have shown that a sudden westward swing of the Pacific Plate by 30–35° at the latitude of Hawaii can be caused by the demise of the slab pull force from intraoceanic subduction in the northern Pacific around the HEB time. This amount of change in Pacific Plate motion is similar to those constrained by recent plate circuit analyses[9,10] (Fig. 4). The bend describes an anticlockwise swing of about 60°. Therefore, our results suggest that the remaining 25–30° of the bend angle are caused by hotspot drift in response to a change in mantle convection[3]. The computed residual hotspot drift requires a southward motion of ~1,200 km, especially between about 80 and 40 Ma (Fig. 4), consistent with palaeomagnetic constraints[3,8] and geodynamic models[5] (Extended Data Fig. 8).

The required change in mantle flow may have its origin in capture and release of the Hawaiian plume by the rapidly moving Pacific–Kula spreading centre[33] or through the combination of Pacific Plate motion, shearing of the upper mantle and deep mantle advection of the plume source[4,5]. On the basis of our geodynamic models, we suggest that an anticlockwise change in the shearing of the upper mantle between 50 and 47 Ma combined with a change in the southward motion direction and rate in the deep lower mantle (Extended Data Fig. 9) may account for the mantle flow component of the HEB.

The drift of the hotspot and change in plate motion could have the same underlying mechanism. Demise of Kronotsky subduction reduced the northward pull such that the existing pull from the west started to dominate the force balance; a commensurate strong change occurred in the shearing of the upper mantle as these forces were rearranged. The models suggest that the mantle and the plates make roughly equal contributions to major plate tectonic events, reflecting their close coupling as two parts of the same system. With this concept and the new capabilities in geodynamics, a window now opens to address potentially even more profound tectonic changes, including the 100 Ma event expressed in changes of fracture zone orientations seen globally[34]. We are on the cusp of understanding such changes quantitatively from a dynamic perspective.

Online content

Any methods, additional references, Nature Research reporting summaries, source data, extended data, supplementary information, acknowledgements, peer review information; details of author contributions and competing interests; and statements of data and code availability are available at https://doi.org/10.1038/s41561-021-00862-6.

Received: 21 November 2020; Accepted: 29 October 2021;
Published online: 23 December 2021

References

1. Morgan, W. J. Deep mantle convection plumes and plate motions. *Bull. Am. Assoc. Pet. Geol.* **56**, 203–213 (1972).
2. Torsvik, T. H. et al. Pacific plate motion change caused the Hawaiian–Emperor Bend. *Nat. Commun.* **8**, 15660 (2017).
3. Tarduno, J. A. et al. The Emperor seamounts: southward motion of the Hawaiian hotspot plume in Earth's mantle. *Science* **301**, 1064–1069 (2003).
4. Steinberger, B., Sutherland, R. & O'Connell, R. J. Prediction of Emperor–Hawaii seamount locations from a revised model of global plate motion and mantle flow. *Nature* **430**, 167–173 (2004).
5. Hassan, R., Müller, R. D., Gurnis, M., Williams, S. E. & Flament, N. A rapid burst in hotspot motion through the interaction of tectonics and deep mantle flow. *Nature* **533**, 239–242 (2016).
6. Wessel, P. & Kroenke, L. W. Pacific absolute plate motion since 145 Ma: an assessment of the fixed hot spot hypothesis. *J. Geophys. Res. Solid Earth* **113**, B6 (2008).
7. Torsvik, T. H. et al. Pacific–Panthalassic reconstructions: overview, errata and the way forward. *Geochem. Geophys. Geosyst.* **20**, 3659–3689 (2019).
8. Bono, R. K., Tarduno, J. A. & Bunge, H.-P. Hotspot motion caused the Hawaiian–Emperor Bend and LLSVPs are not fixed. *Nat. Commun.* **10**, 3370 (2019).
9. Müller, R. D. et al. Global-scale plate reorganization events since Pangea breakup. *Annu. Rev. Earth Planet. Sci.* **44**, 107–138 (2016).
10. Müller, R. D. et al. A global plate model including lithospheric deformation along major rifts and orogens since the Triassic. *Tectonics* **38**, 1884–1907 (2019).
11. Reagan, M. et al. Forearc ages reveal extensive short-lived and rapid seafloor spreading following subduction initiation. *Earth Planet. Sci. Lett.* **506**, 520–529 (2019).
12. Sutherland, R. et al. Continental scale of geographic change across Zealandia during subduction zone initiation. *Geology* **48**, 419–424 (2020).
13. Whittaker, J. et al. Major Australian–Antarctic plate reorganization at Hawaiian–Emperor Bend time. *Science* **318**, 83–86 (2007).
14. Patriat, P. & Achache, J. India–Eurasia collision chronology has implications for crustal shortening and driving mechanism of plates. *Nature* **311**, 615–621 (1984).
15. Richards, M. A. & Lithgow-Bertelloni, C. Plate motion changes, the Hawaiian–Emperor Bend, and the apparent success and failure of geodynamic models. *Earth Planet. Sci. Lett.* **137**, 19–27 (1996).
16. Müller, R. D., Sdrolias, M., Gaina, C., Steinberger, B. & Heine, C. Long-term sea-level fluctuations driven by ocean basin dynamics. *Science* **319**, 1357–1362 (2008).
17. Faccenna, C., Becker, T. W., Lallemand, S. & Steinberger, B. On the role of slab pull in the Cenozoic motion of the Pacific Plate. *Geophys. Res. Lett.* **39**, L03305 (2012).
18. Conrad, C. P. & Lithgow-Bertelloni, C. How mantle slabs drive plate tectonics. *Science* **298**, 207–209 (2002).
19. Buffett, B. A. Plate force due to bending at subduction zones. *J. Geophys. Res. Solid Earth* **111**, B9 (2006).
20. Forsyth, D. & Uyeda, S. On the relative importance of the driving forces of plate motion. *Geophys. J. Int.* **43**, 163–200 (1975).
21. Billen, M. I. Modeling the dynamics of subducting slabs. *Annu. Rev. Earth Planet. Sci.* **36**, 325–356 (2008).
22. Stadler, G. et al. The dynamics of plate tectonics and mantle flow: from local to global scales. *Science* **329**, 1033–1038 (2010).
23. Taylor, B. The single largest oceanic plateau: Ontong Java–Manihiki–Hikurangi. *Earth Planet. Sci. Lett.* **241**, 372–380 (2006).
24. Levashova, N. M., Shapiro, M. N., Beniamovsky, V. N. & Bazhenov, M. L. Paleomagnetism and geochronology of the Late Cretaceous–Paleogene island arc complex of the Kronotsky Peninsula, Kamchatka, Russia: kinematic implications. *Tectonics* **19**, 834–851 (2000).
25. Konstantinovskaya, E. in *Arc–Continent Collision* (eds Brown D. & Ryan, P. D.) 247–277 (Springer, 2011).
26. Rudi, J. et al. An extreme-scale implicit solver for complex PDEs: highly heterogeneous flow in Earth's mantle. In *Proc. International Conference for High Performance Computing, Networking, Storage, and Analysis* (Association for Computing Machinery, 2015).
27. Bakhteev, M., Morozov, O. & Tikhomirova, S. Structure of the eastern Kamchatka ophiolite-free collisional suture–Grechishkin thrust. *Geotectonics* **31**, 236–246 (1997).
28. Domeier, M. et al. Intraoceanic subduction spanned the Pacific in the Late Cretaceous–Paleocene. *Sci. Adv.* **3**, eaao2303 (2017).
29. Vaes, B., Van Hinsbergen, D. J. & Boschman, L. M. Reconstruction of subduction and back-arc spreading in the NW Pacific and Aleutian basin: clues to causes of Cretaceous and Eocene plate reorganizations. *Tectonics* **38**, 1367–1413 (2019).
30. Seton, M. et al. Melanesian back-arc basin and arc development: constraints from the eastern Coral Sea. *Gondwana Res.* **39**, 77–95 (2016).
31. Leng, W. & Gurnis, M. Subduction initiation at relic arcs. *Geophys. Res. Lett.* **42**, 7014–7021 (2015).
32. Faccenna, C., Holt, A. F., Becker, T. W., Lallemand, S. & Royden, L. H. Dynamics of the Ryukyu/Izu–Bonin–Marianas double subduction system. *Tectonophysics* **746**, 229–238 (2018).
33. Tarduno, J., Bunge, H.-P., Sleep, N. & Hansen, U. The bent Hawaiian–Emperor hotspot track: inheriting the mantle wind. *Science* **324**, 50–53 (2009).
34. Matthews, K. J., Seton, M. & Müller, R. D. A global-scale plate reorganization event at 105–100 Ma. *Earth Planet. Sci. Lett.* **355**, 283–298 (2012).

Methods

Plate reconstructions. *Pacific Plate motion constrained by plate reconstructions.* Plate reconstructions suggest a non-trivial change in the direction of Pacific Plate motion at the time of the HEB, although some differences exist in terms of the degrees of the change[7]. These reconstructions can be categorized into two main groups, those with reference to the hotspots in the Pacific realm and those in the Indo-Atlantic realm. In the Pacific realm, assuming fixed or moving hotspots, the Pacific Plate motion is inferred by fitting the age and the geometry of hotspot tracks in the Pacific[6,35]. These models suggest a substantial change of Pacific Plate motion at the time of the HEB. However, because the motion of the Hawaiian hotspot is debated and to better discern the Pacific Plate motion history, relative plate circuits are used to link the Pacific to the Indo-Atlantic realm. Using the plate circuit through West–East Antarctica, some earlier models, for example Seton et al.[36] and model 1 in Steinberger et al.[4], predict a minor change of Pacific Plate motion at around 47 Ma. This relative plate circuit is not well constrained[37]. It can induce unreasonable motion between the North and South islands of New Zealand, unless carefully calibrated to minimize divergent or convergent motion between the North and South islands of New Zealand[37]. When the up-to-date spreading history for Australia–East Antarctica[38] and the East–West Antarctica rotations of Granot et al.[39] are used, as implemented in the two successive models of Müller et al.[9,10], the Pacific Plate motion is inferred to change its direction substantially at 47 Ma. However, an alternative plate circuit through Australia–Lord Howe Rise has also been suggested[40], keeping the Lord Howe Rise fixed to the Pacific Plate before the HEB. The rationale for this solution has been put in question by ref. [41], who documented geological evidence for a plate boundary running through New Zealand before the HEB, called the 'proto Alpine Fault', which would have continued north of Zealand, separating the Lord Howe Rise from the Pacific Plate. Nevertheless, plate reconstructions implemented with this plate circuit also yield a substantial change in Pacific Plate motion at 47 Ma in both fixed and moving hotspot reference frames[7]. In Figs. 3 and 4, we show the reconstructions by Müller et al.[9,10], Torsvik et al.[7] and Bono et al.[8], with Müller et al. using the updated West–East Antarctic circuit and the latter two using the Australia–Lord Howe Rise circuit.

Plate reconstructions used for the geodynamic models. Changes were made to the standard reconstruction of ref. [9] to reflect recent updates in our understanding of IBM and Tonga–Kermadec subduction initiation while isolating the influence of subduction initiation on Pacific Plate motion. The Tonga–Kermadec subduction was eliminated for ages of 50 Ma and earlier to reflect the most recent seismic and ocean drilling results[12,42]. At 50 Ma, the nascent IBM slab was excluded to maximize the northward force on the Pacific Plate. Then in subsequent models, the IBM slab was progressively added to reflect the 52 Ma age of initiation from recent drilling on the IBM forearc[11], thereby allowing isolation of IBM initiation on plate motion.

We revised the global reconstruction[9] to incorporate the intraoceanic subduction system in the northern Pacific since Late Cretaceous as described in the main text. The position of the Kronotsky arc was taken from palaeomagnetic arguments[24]. The pre-Palaeocene arc was stationary in palaeolatitude or moving slowly southwards[24], implying a northward subduction as the Kronotsky arc could not reside on either the Pacific or Kula plate as both rapidly moved towards the north. We adopted a scenario where the Kronotsky arc resided in the oceanic periphery of the slowly moving Eurasian Plate while the Pacific Plate was subducting beneath it (Fig. 1d). This scenario provided the northward slab pull force for the Pacific Plate. Since the Eocene, before the collision of the Kronotsky arc with Kamchatka in the late Miocene, the Kronotsky arc had a similar northward motion with the Pacific Plate[24], suggesting the Pacific Plate no longer subducted beneath the arc. Subduction-related volcanism was active until the late Eocene[24,25]. We thus adopted a scenario where a southward subduction beneath the arc occurred for the short period before the extinction of the arc around the late Eocene, and the arc was soon captured by the Pacific Plate afterwards. We infer that subduction polarity reversal occurred at around 50 Ma, which caused the demise of the earlier Kronotsky subduction and the abrupt change in Pacific Plate motion. Such a polarity reversal could be induced by the subduction of a bathymetric anomaly, such as a relic island arc or oceanic plateau.

With the plate kinematics, we built the age grids of the seafloor (Fig. 1d–f) using a tracer-based algorithm detailed in ref. [43].

Palaeomantle structure. With the plate reconstructions, we used a workflow to construct the ancient thermal structures as a combination of lithosphere, upper-mantle slabs and lower-mantle thermal structures. Following Stadler et al.[22], a half-space cooling model defines the thermal structure of the oceanic lithosphere with seafloor ages from the plate reconstructions. We assigned cratons the thermal age of 300 Ma, regions near the subduction zones 75 Ma and remaining continental regions 125 Ma.

Upper-mantle slabs. We implement a kinematic tool with the Python package pyGPlates to construct upper-mantle slabs at specific ages with the slab age and length constrained by plate reconstructions. With the history of plate motions and seafloor ages from plate reconstructions, the amount and ages of subducted plates were computed for each age of interest, for example, 47 Ma (Extended Data Fig. 1a). A slab surface was computed by projecting this slab to depth (Extended Data Fig. 1b) using empirical relations that fit present-day slabs[44]. For simplicity, we define one shallow dip to be the dip from the trench to 125 km depth, and one deep dip from 125 km to 400 km. Utilizing the dataset that summarizes the present-day slab dips and subduction parameters[44], we derived the empirical relation between the two dips and subduction parameters:

$$\alpha_s = 42 - 0.067 \times A_{\mathrm{sub}} - 7.2 \times \mathrm{OPN} \quad (1)$$

$$\alpha_d = 73 - 0.07 \times A_{\mathrm{sub}} - 7.1 \times \mathrm{OPN} \quad (2)$$

where α_s is the shallow dip, α_d the deep dip, A_{sub} the duration of subduction and OPN the nature of the overriding plate, with OPN = 1 representing continental plate and OPN = 0 representing oceanic plate. The dip angles of the Farallon flat slab cannot be fully captured by this empirical relation, so a flat slab geometry for the Farallon slab was prescribed between 30° and 45° N (Extended Data Fig. 1b,c) that roughly corresponds to the Laramide Orogeny[45], similar to that in ref. [46]. However, the geometry of the Farallon slab does not have an impact on Pacific Plate motion because forces on the Farallon Plate do not propagate to the Pacific Plate due to the Farallon–Pacific spreading centre.

To ensure a smooth slab profile, a second-order polynomial fit was used to interpolate the slab surface with the given shallow and deep dips. This procedure provides an excellent fit to present-day seismically defined slabs[44]. With the slab surface and associated thermal ages, the thermal structure of slabs was computed with the initial half-space-cooling lithosphere entering the mantle and with diffusion and advection parameterized as in ref. [46].

Lower-mantle thermal structure. The lower-mantle structure was computed by using the finite element method in a spherical geometry[47] with plate subduction since 230 Ma and data assimilation[46,48]. Thermal-chemical convection with imposed velocity and temperature boundary conditions was computed with surface velocities from the plate reconstruction. The method has been validated by comparison with present-day mantle seismic structure, including slabs[48] and large low-shear-velocity provinces[5]. We take the lower-mantle slab structure at the target age (say, 47 Ma) from these data-assimilation models as an essential part of the input temperature field.

We blended the lithosphere, upper-mantle slabs and lower-mantle structure to create global thermal structures (Extended Data Fig. 2). The workflow not only has a consistent thermal flux in subduction zones but leads to realistic slab geometries with predicted plate motions that fit global plate kinematics (Fig. 2d–f). The upper-mantle slabs are not taken from the data-assimilation/convection models as their limited resolution leads to upper-mantle slabs that are usually too thick to generate reasonable representations of the hinge zone of subducted plates.

Plume-head push. We computed a series of models that considered the influence of the eruption of the combined Ontong Java–Manihiki–Hikurangi plateaus at about 120 Ma[23]. We have approximated this with a flattened plume head below the centre of the combined plateau in the reconstructions (Extended Data Fig. 4b)[9]. Estimates for the largest flattened plume heads in the Atlantic and Indian oceans are 2,000–2,500 km in diameter, 175 km in thickness (depth) and with a temperature anomaly of 200–400 °C[49]. We purposely overestimated the flattened plume head in the Pacific using 3,000 km diameter, 300 km thickness and 500 °C temperature anomaly (Extended Data Fig. 4a, b). Coincidentally, the position of the inserted plume head was underlain by a plume tail down to the position of the large low-shear-velocity province edge. This thermal structure at 120 Ma was integrated forwards (Extended Data Fig. 4c) with CitcomS and data assimilation[44] as detailed in the preceding.

The resultant thermal structure at 50 Ma was compared with that without the initial plume head (Extended Data Fig. 4c,d). The difference represents the contribution from the plume head. We superimposed this difference onto the thermal structure of MT50 (Supplementary Table 1), the comparison model, to create the thermal structure of MT50pl, the test model, to show the effect of the plume head on Pacific Plate motion (Extended Data Fig. 4e).

Ultra-high-resolution forward models. The palaeothermal structures were used in well-resolved computations of plate motions and mantle flow, generally following those for the present day as detailed in ref. [22].

Weak zones and adaptive mesh refinement. The shape and curvature of the weak zones were taken from the same surface used for thermal slabs, as just described; consequently, the weak zones are self–consistent with thermal slabs such that thermal (and hence, mechanical) slab and weak zone gradually curve together, as they do in models with tight coupling between shear zone development, slab mechanics and thermal evolution[50,51]. This is an important improvement over the earlier high-resolution models[22]. To ensure that weak zones, the finest structures in the global models, are resolved in the numerical models, we used adaptive mesh refinement. The weak zones were resolved with an element size of ~2 km (and with quadratic elements (see the following), the resolution is ~1 km). Within the weak zone, the viscosity was multiplied by a factor (see ref. [22])

$$f(d) = 1 - (1 - w)\exp\left(-\frac{\max(0, d - \sigma)}{2\sigma^2}\right), \tag{3}$$

where d is the distance to the centre of the weak zone, w is the weak-zone factor and σ is the weak-zone width (Supplementary Table 2). Each weak zone has a viscosity reduction factor (see ref. [22]) of nominally $w = 10^{-5}$. Any deviations from these values are given in Supplementary Table 1.

Viscosity. The non-dimensional upper-mantle and lower-mantle viscosity is controlled by dislocation creep and diffusion creep, respectively:

$$\eta_{\mathrm{df,ds}} = A(r)\dot{\varepsilon}_{\mathrm{II}}^{\frac{1-n}{n}} \exp(E_a(0.5 - T)/n) \tag{4}$$

Where $\dot{\varepsilon}_{\mathrm{II}}$ is the second invariant of the strain rate tensor, T the temperature, $A(r)$ the viscosity prefactor, n the stress exponent and E_a the activate energy (Supplementary Table 2). A yield criterion was applied to obtain the effective viscosity:

$$\eta_{\mathrm{eff}} = \min\left(\frac{\sigma_y}{\dot{\varepsilon}_{\mathrm{II}}}, \eta_{\mathrm{df,ds}}\right) \tag{5}$$

where σ_y is the yield stress.

Solution of the forward problem. The discretization of Earth's mantle was carried out by finite elements on aggressively adaptively refined hexahedral meshes. We used a quadratic finite element approximation for the velocity and linear elements for the pressure. To distribute the discrete problem onto distributed-memory parallel computing clusters, parallel forest-of-octrees algorithms were used for efficient, scalable mesh refinement/coarsening, mesh balancing and repartitioning[52]. The large implicit nonlinear systems to be solved are poorly conditioned, and specifically tailored iterative numerical methods including advanced preconditioning techniques are required. Our hybrid spectral–geometric–algebraic multigrid (HMG) method constitutes a core preconditioning component of the solver[26,53]. HMG is essential for preconditioning efficacy (reducing iteration counts) and algorithmic and parallel scalability to extreme scales of 10^6 processor cores. In addition, we used a preconditioner for the Schur complement[54] that is robust in the presence of the highly heterogeneous viscosities present in the models. Combining this Schur complement preconditioner with HMG results in a scalable and highly robust implicit linear solver. The implicit linear solver was embedded into an inexact Newton–Krylov method to deal with severely nonlinear rheologies[26]. We developed a nonlinear preconditioner[55] to avoid prohibitively stagnating convergence of Newton's method due to highly nonlinear physics at plate fault zones.

Data availability

The raw data for the paper have been deposited on Caltech Data (https://doi.org/10.22002/D1.2150), including the digitized alternative plate reconstruction and the predicted plate motion. The authors declare that all other data supporting the findings of this study are available within the paper and its Supplementary Information files with their sources annotated in the text.

Code availability

The plate kinematic tool GPlates and its python version can be accessed at www.gplates.org/. The original version of CitcomS is available at www.geodynamics.org/cig/software/citcoms/. The adaptive nonlinear Stokes solver (Rhea) used to predict plate motion is available upon request.

References

35. Steinberger, B. & Gaina, C. Plate-tectonic reconstructions predict part of the Hawaiian hotspot track to be preserved in the Bering Sea. *Geology* **35**, 407–410 (2007).
36. Seton, M. et al. Global continental and ocean basin reconstructions since 200 Ma. *Earth Sci. Rev.* **113**, 212–270 (2012).
37. Matthews, K. J. et al. Geologic and kinematic constraints on Late Cretaceous to mid Eocene plate boundaries in the southwest Pacific. *Earth Sci. Rev.* **140**, 72–107 (2015).
38. Whittaker, J. M., Williams, S. E. & Müller, R. D. Revised tectonic evolution of the eastern Indian Ocean. *Geochem. Geophys. Geosyst.* **14**, 1891–1909 (2013).
39. Granot, R., Cande, S., Stock, J. & Damaske, D. Revised Eocene–Oligocene kinematics for the West Antarctic rift system. *Geophys. Res. Lett.* **40**, 279–284 (2013).
40. Doubrovine, P. V. & Tarduno, J. A. A revised kinematic model for the relative motion between Pacific oceanic plates and North America since the Late Cretaceous. *J. Geophys. Res. Solid Earth* **113**, 2 (2008).
41. Mortimer, N. Evidence for a pre-Eocene proto-Alpine Fault through Zealandia. *N. Z. J. Geol. Geophys.* **61**, 251–259 (2018).
42. Sutherland, R. et al. Widespread compressional faulting associated with forced Tonga–Kermadec subduction initiation. *Geology* **45**, 355–358 (2017).
43. Karlsen, K. S., Domeier, M., Gaina, C. & Conrad, C. P. A tracer-based algorithm for automatic generation of seafloor age grids from plate tectonic reconstructions. *Comput. Geosci.* **140**, 104508 (2020).
44. Hu, J. & Gurnis, M. Subduction duration and slab dip. *Geochem. Geophys. Geosyst.* **21**, e2019GC008862 (2020).
45. Coney, P. J. & Reynolds, S. J. Cordilleran Benioff zones. *Nature* **270**, 403–406 (1977).
46. Bower, D. J., Gurnis, M. & Flament, N. Assimilating lithosphere and slab history in 4-D Earth models. *Phys. Earth Planet. Inter.* **238**, 8–22 (2015).
47. Zhong, S., Zuber, M. T., Moresi, L. N. & Gurnis, M. The role of temperature-dependent viscosity and surface plates in spherical shell models of mantle convection. *J. Geophys. Res.* **105**, 11063–11082 (2000).
48. Hu, J., Liu, L. & Zhou, Q. Reproducing past subduction and mantle flow using high-resolution global convection models. *Earth Planet. Phys.* **2**, 189–207 (2018).
49. Campbell, I. & Griffiths, R. Implications of mantle plume structure for the evolution of flood basalts. *Earth Planet. Sci. Lett.* **99**, 79–93 (1990).
50. Mao, X., Gurnis, M. & May, D. A. Subduction initiation with vertical lithospheric heterogeneities and new fault formation. *Geophys. Res. Lett.* https://doi.org/10.1002/2017GL075389 (2017).
51. Zhong, X. & Li, Z. Forced subduction initiation at passive continental margins: velocity-driven versus stress-driven. *Geophys. Res. Lett.* **46**, 11054–11064 (2019).
52. Burstedde, C., Wilcox, L. C. & Ghattas, O. p4est: scalable algorithms for parallel adaptive mesh refinement on forests of octrees. *SIAM J. Sci. Comput.* **33**, 1103–1133 (2011).
53. Sundar, H. et al. Parallel geometric–algebraic multigrid on unstructured forests of octrees in SC12. In *Proc. International Conference for High Performance Computing, Networking, Storage and Analysis* (Association for Computing Machinery, 2012).
54. Rudi, J., Stadler, G. & Ghattas, O. Weighted BFBT preconditioner for Stokes flow problems with highly heterogeneous viscosity. *SIAM J. Sci. Comput.* **39**, S272–S297 (2017).
55. Rudi, J., Shih, Y.-h. & Stadler, G. Advanced Newton methods for geodynamical models of Stokes flow with viscoplastic rheologies. *Geochem. Geophys. Geosyst.* https://doi.org/10.1029/2020GC009059 (2020).

Acknowledgements

J.H. and M.G. were partially supported by the US National Science Foundation (NSF) through awards EAR-1645775 and EAR-2009935. J.R. was supported by the US Department of Energy, Office of Science, under contract DE-AC02-06CH11357. G.S. was partially supported by NSF grants EAR-1646337 and DMS-1723211. Computations were carried out on the NSF-supported Stampede-2 and Frontera supercomputers at the Texas Advanced Computer Center under allocations TG-EAR160027, TG-DPP130002 and FTA-SUB-CalTech. The funders had no role in study design, data collection and analysis, decision to publish or preparation of the manuscript.

Author contributions

J.H. and M.G. designed the study. J.H. carried out the numerical experiments. J.R. and G.S. expanded the functionality of the adaptive nonlinear Stokes solver Rhea and provided expertise in scientific computing. R.D.M. helped with plate reconstruction. All authors participated in result interpretation and manuscript preparation.

Competing interests

The authors declare no competing interests.

Additional information

Extended data is available for this paper at https://doi.org/10.1038/s41561-021-00862-6.

Supplementary information The online version contains supplementary material available at https://doi.org/10.1038/s41561-021-00862-6.

Correspondence and requests for materials should be addressed to Jiashun Hu.

Peer review information *Nature Geoscience* thanks Claudio Faccenna and the other, anonymous, reviewer(s) for their contribution to the peer review of this work. Primary Handling Editors: Stefan Lachowycz and Rebecca Neely in collaboration with the *Nature Geoscience* team.

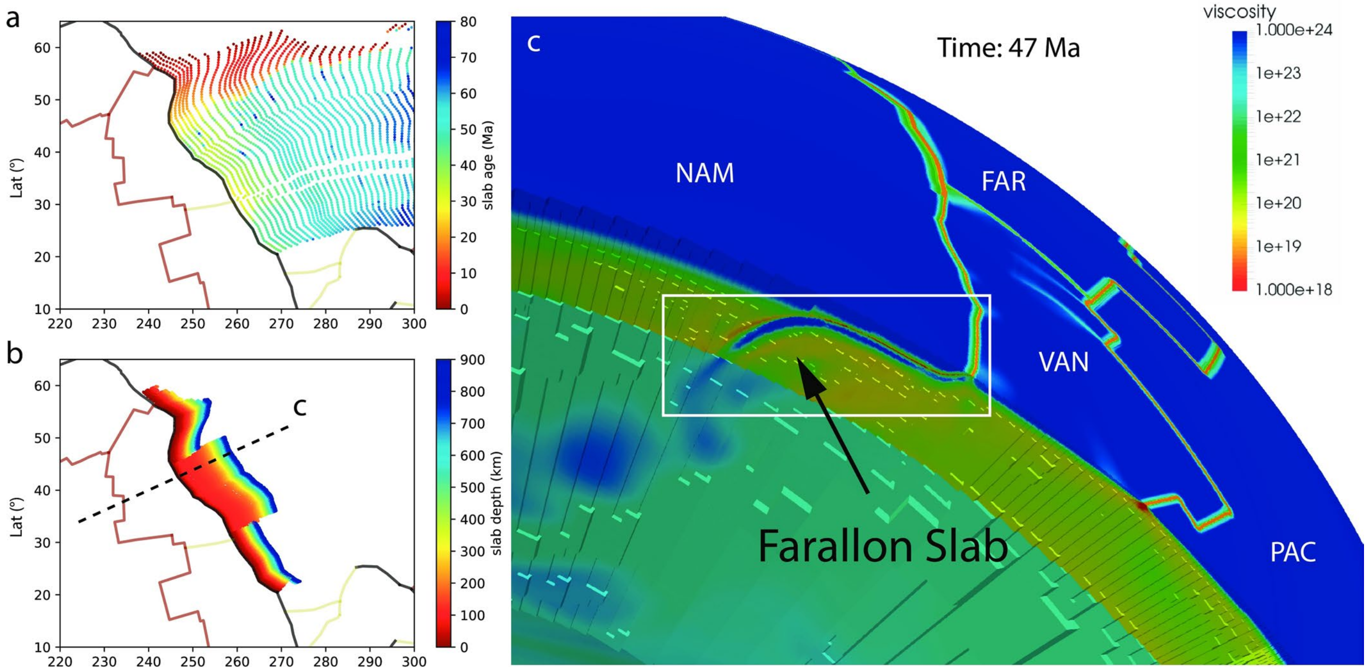

Extended Data Fig. 1 | Representative data showing construction of a paleo slab with pyGplates. Representative data showing construction of a paleo slab with pyGplates. **a**, The thermal age of the lithosphere within the slab. **b**, Depth of the slab. **c**, A cross section of the slab with plates labeled as NAM for North America, FAR for Farallon, VAN for Vancouver and PAC for Pacific. The location is labeled in **b**.

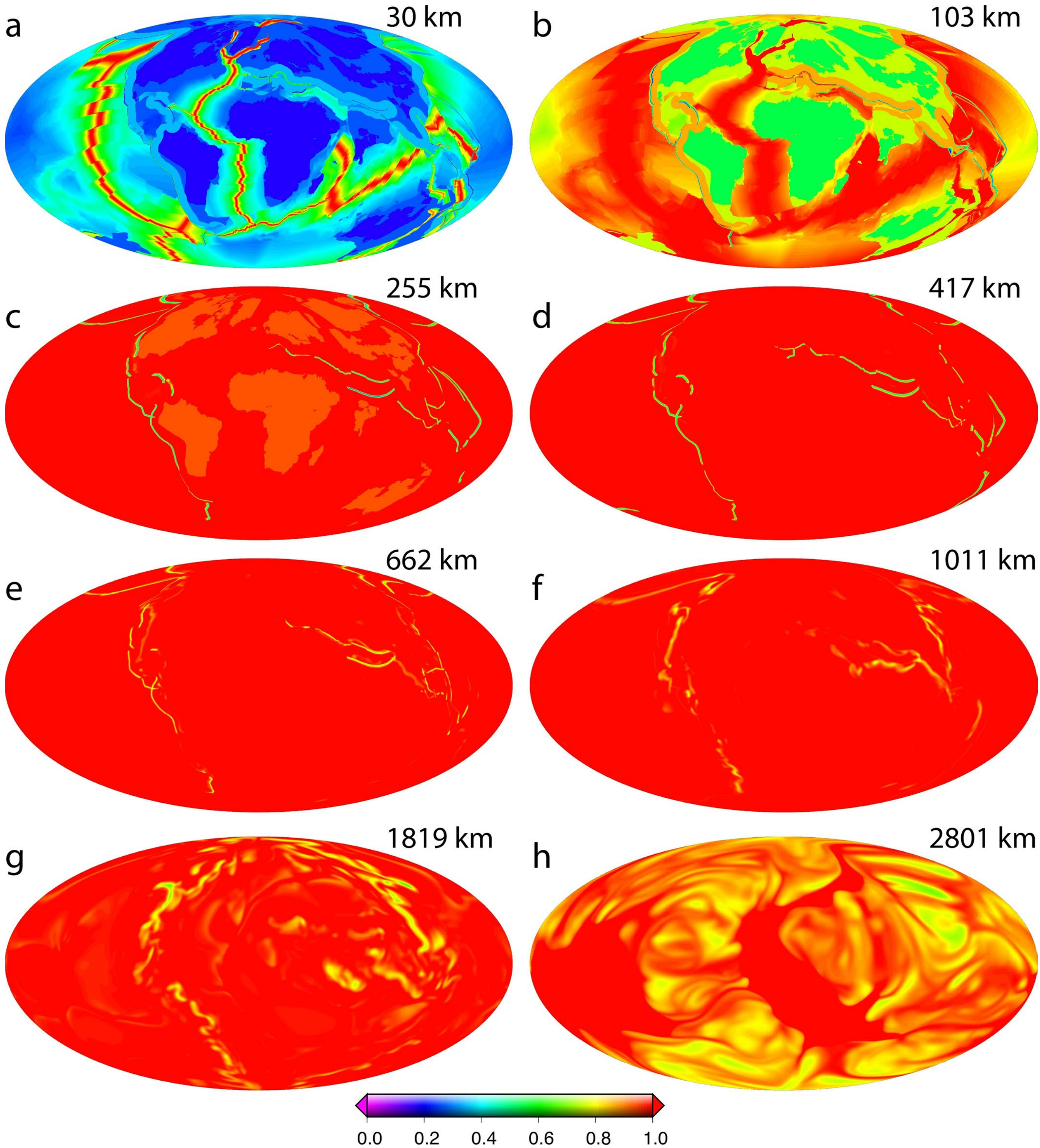

Extended Data Fig. 2 | Representative global thermal structure. Representative global thermal structure. This example shows the input for the geodynamic model based on the traditional plate reconstruction[9] at 47 Ma.

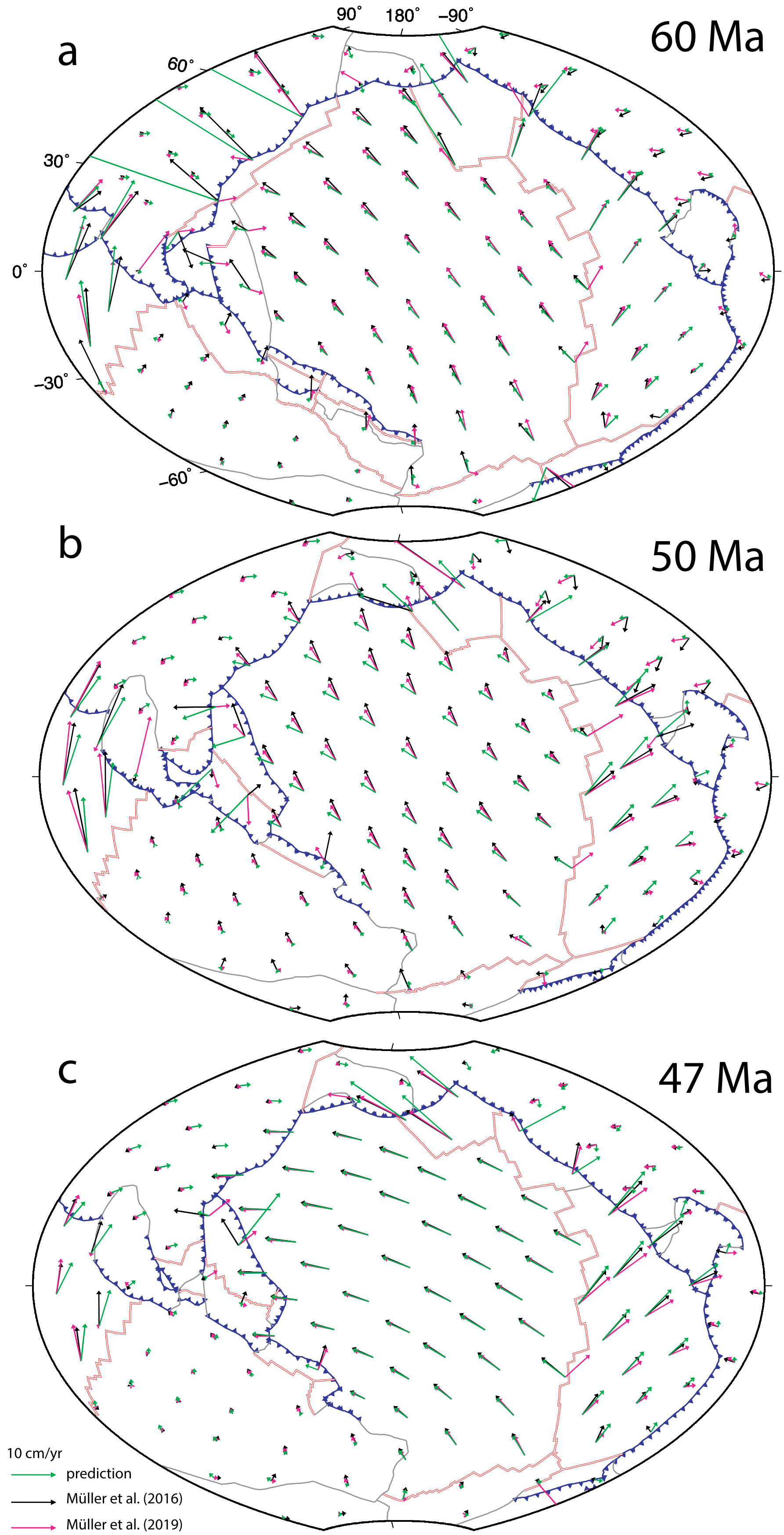

Extended Data Fig. 3 | Predicted plate motion with the traditional plate reconstruction that incorporates the Izanagi-Pacific Ridge subduction. Predicted plate motion at 60 (**a**), 50 (**b**) and 47 (**c**) Ma, based on the traditional plate reconstruction that incorporates the Izanagi-Pacific Ridge subduction.

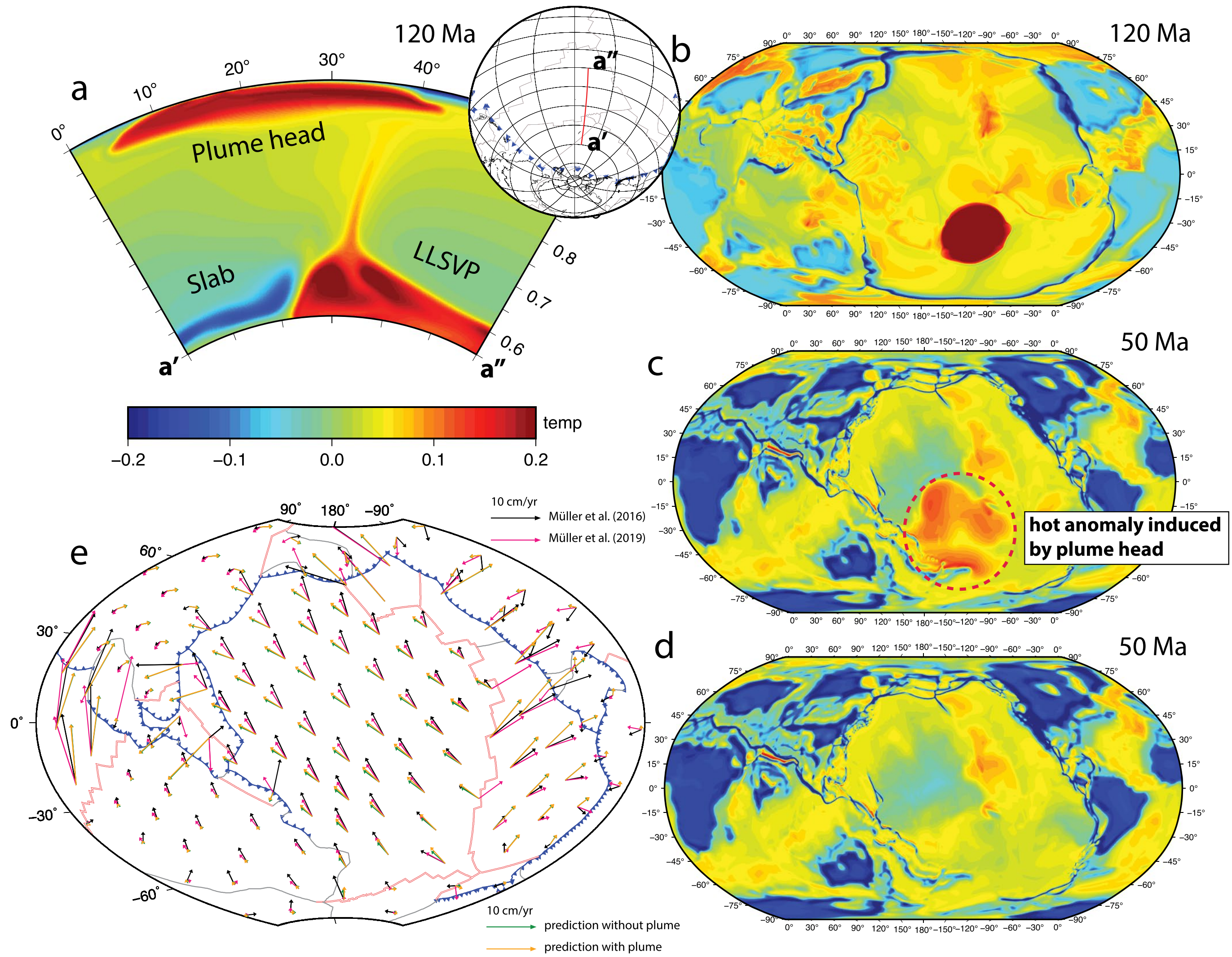

Extended Data Fig. 4 | Model with plume-head push. Model with plume-head push. **a, b** and **c** show the thermal structures of the forward CitcomS model with plume-head. **a** and **b** show a cross section (see the location of the cross section in the inserted panel) and a map view (at 200 km) of the initial plume head at 120 Ma. **c** represents the thermal structure of the forward CitcomS model at 50 Ma. **d** represents the thermal structure of the CitcomS model at 50 Ma without imposing the plume head at 120 Ma. The difference between **c** and **d** represents the contribution from the plume head, which is highlighted with the red circle in **c**. The difference is superimposed on the thermal structure of the forward model at 50 Ma based on the traditional model, to test the effect of plume-head push, which is shown in **e**. In **e**, the green, orange, black and red arrows represent the geodynamically predicted velocities without plume-head push, the geodynamically predicted velocities with plume-head push, the reconstructed velocities from ref. [9] and the reconstructed velocities from ref. [10], respectively.

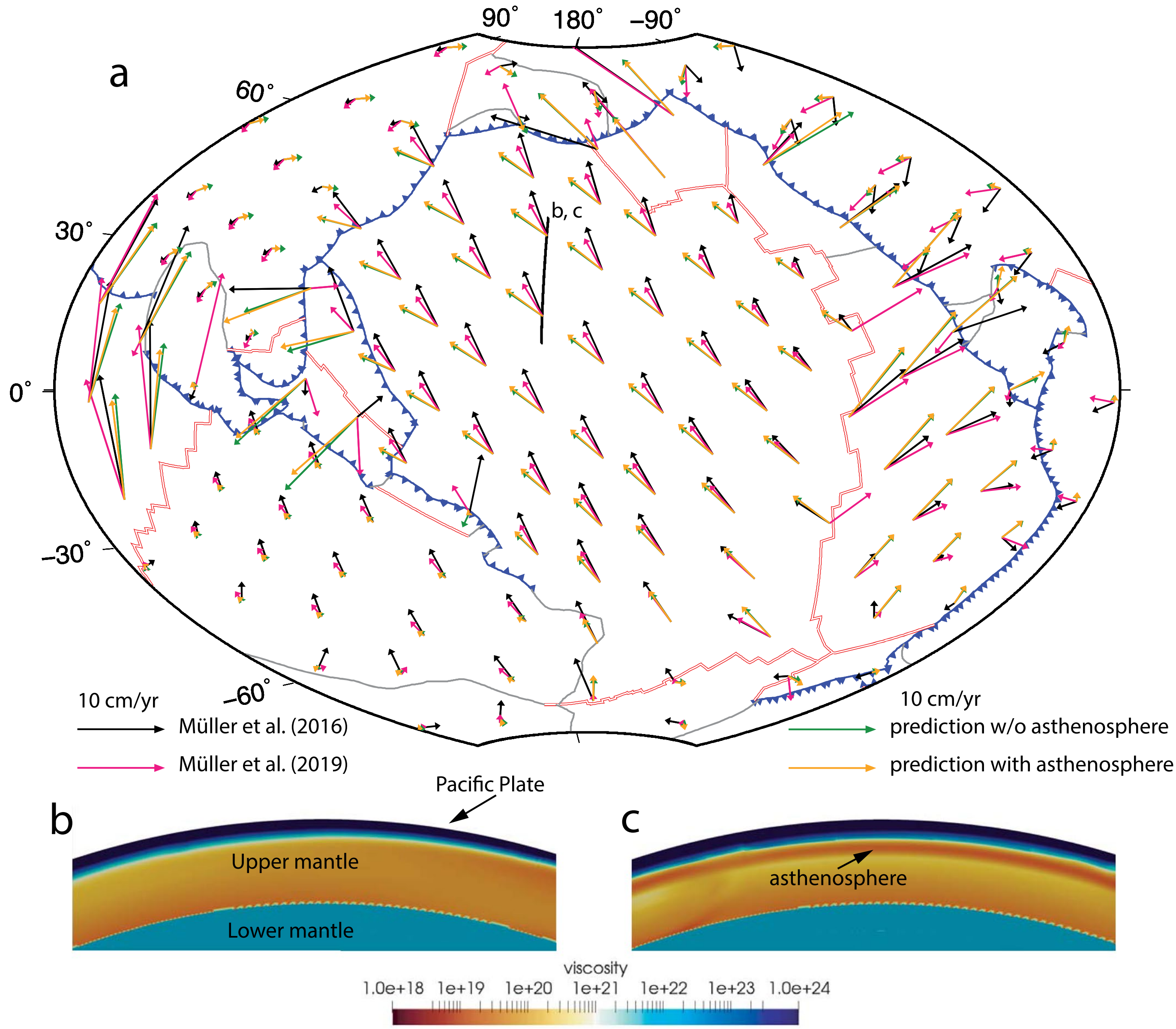

Extended Data Fig. 5 | Comparison of the models with and without asthenosphere. Comparison of the models with (**b**) and without (**c**) asthenosphere. In **a**, the green, orange, black and red arrows represent the geodynamically predicted velocities without asthenosphere, the geodynamically predicted velocities with asthenosphere, the reconstructed velocities from ref. [9] and the reconstructed velocities from ref. [10], respectively.

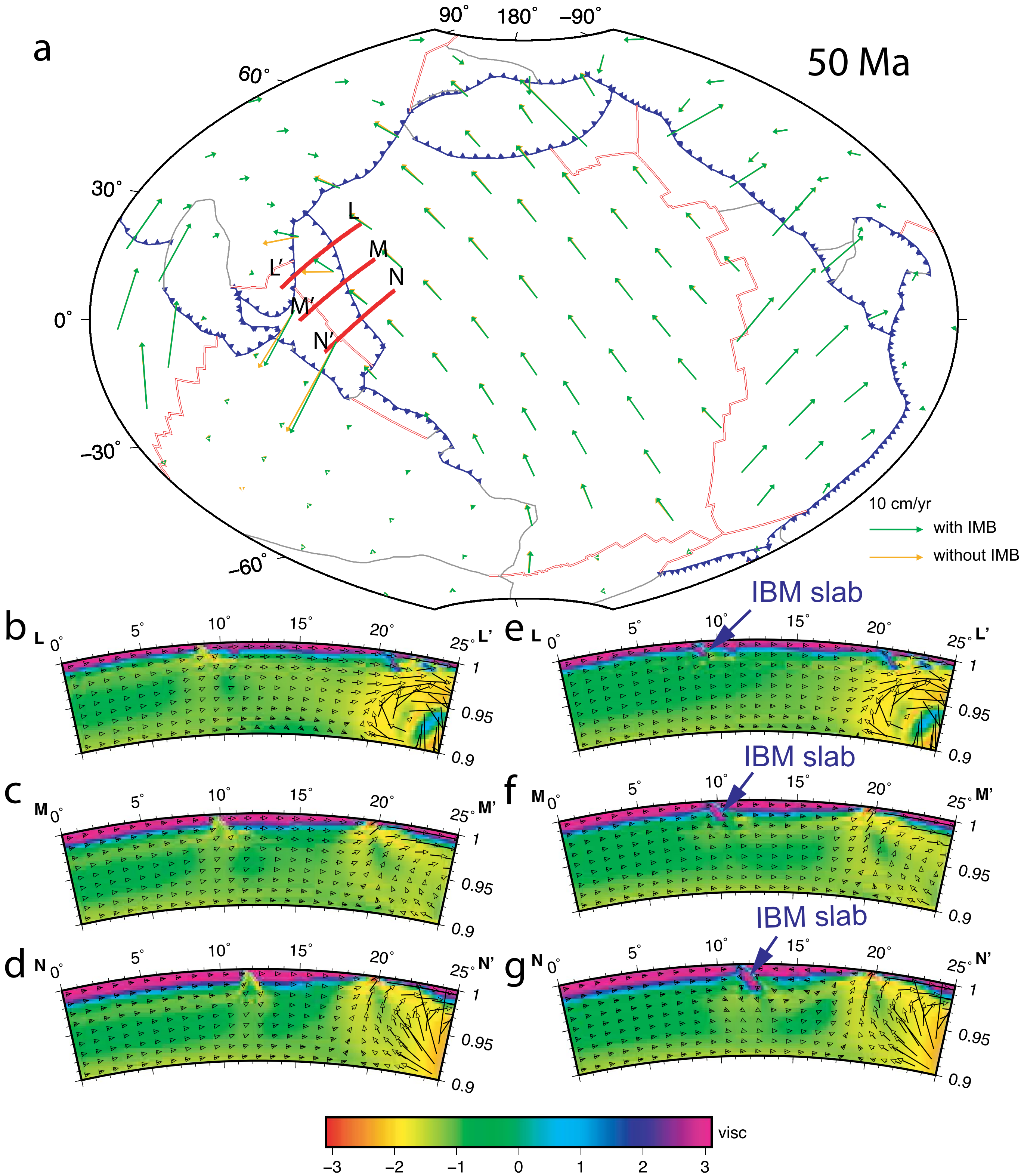

Extended Data Fig. 6 | Testing the effect of the nascent IBM slab at 50 Ma. Testing the effect of the nascent IBM slab at 50 Ma. **a** shows the predicted plate motion for the models with the nascent IBM slab (green arrows) and without the nascent IBM slab (orange arrows). **b, c** and **d** show the viscosity along the cross sections labeled in **a** for the model without the IBM slab. **e, f** and **g** show the viscosity along the cross sections labeled in **a** for the model with the IBM slab.

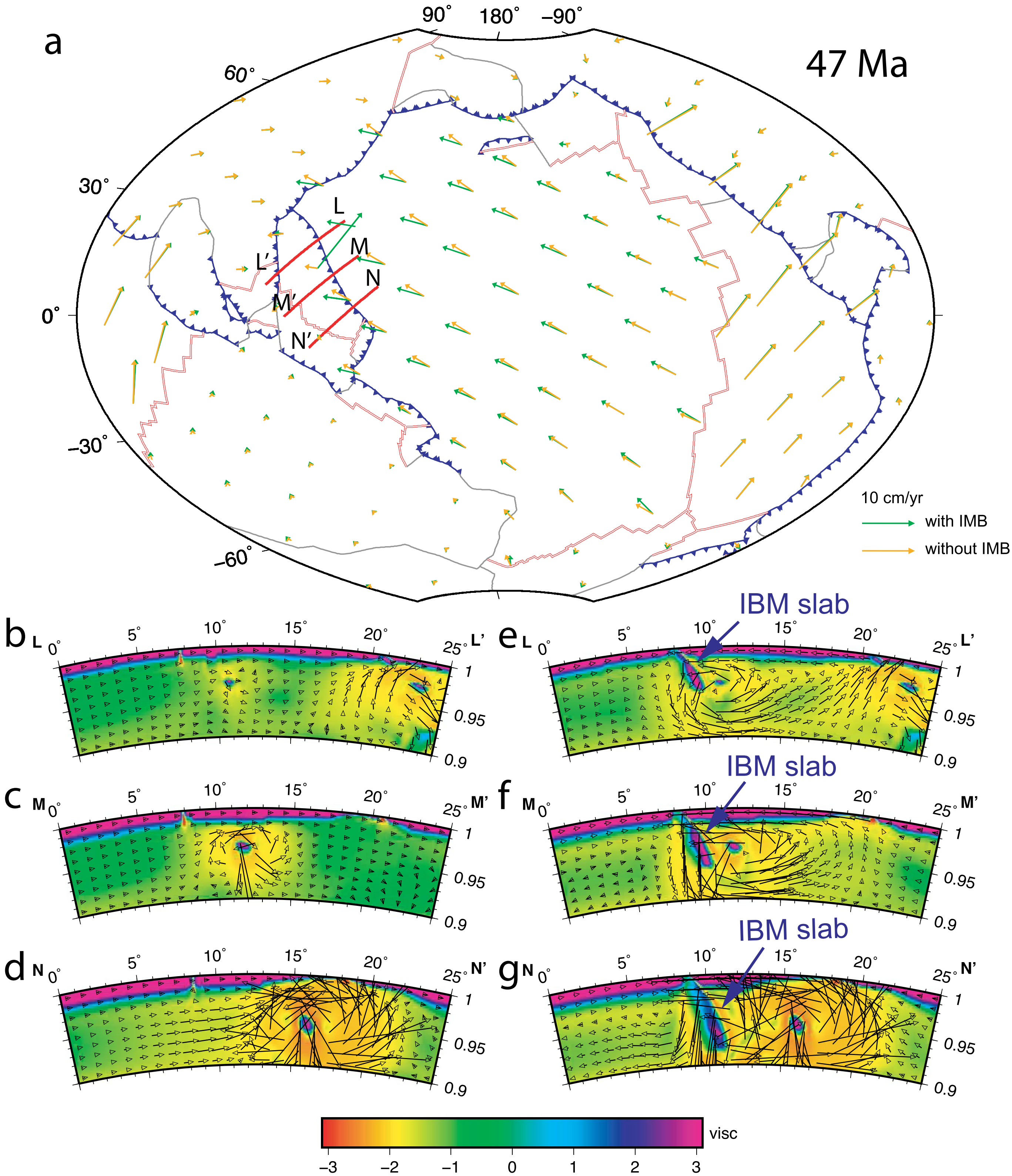

Extended Data Fig. 7 | Testing the effect of nascent IBM slab at 47 Ma. Same as Extended Data Fig. 6, but testing the effect of nascent IBM slab at 47 Ma.

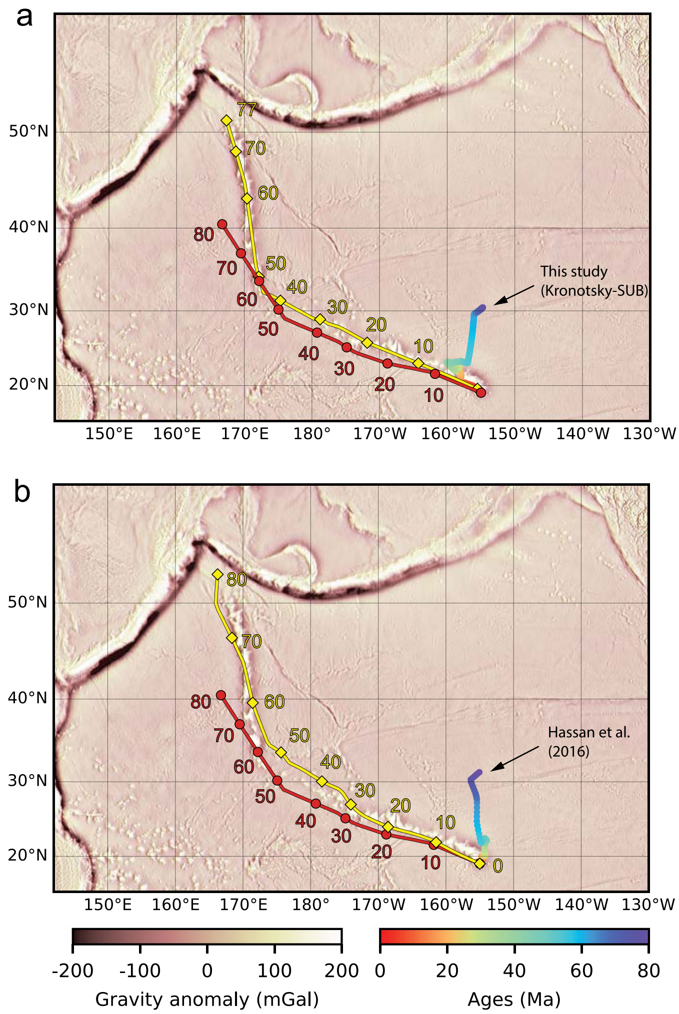

Extended Data Fig. 8 | Computations of the Hawaiian-Emperor Seamount hotspot tracks and plume motion. Computations of the Hawaiian-Emperor Seamount hotspot tracks and plume motion. We combine the Pacific Plate motion change and the hotspot drift path to reconstruct the Hawaiian-Emperor Seamount chain. For the Pacific Plate motion, we use the preferred geodynamic Kronotsky-SUB track that combines the Pacific Plate motion from Müller et al.[9] after 47 Ma and from the geodynamic models that incorporates the Kronotsky subduction before 47 Ma. The residual hotspot drift path in Fig. 4 is used in **a**, while the hotspot drift in Hassan et al.[5] is used in **b**. To first order, the two hotspot drift paths are similar.

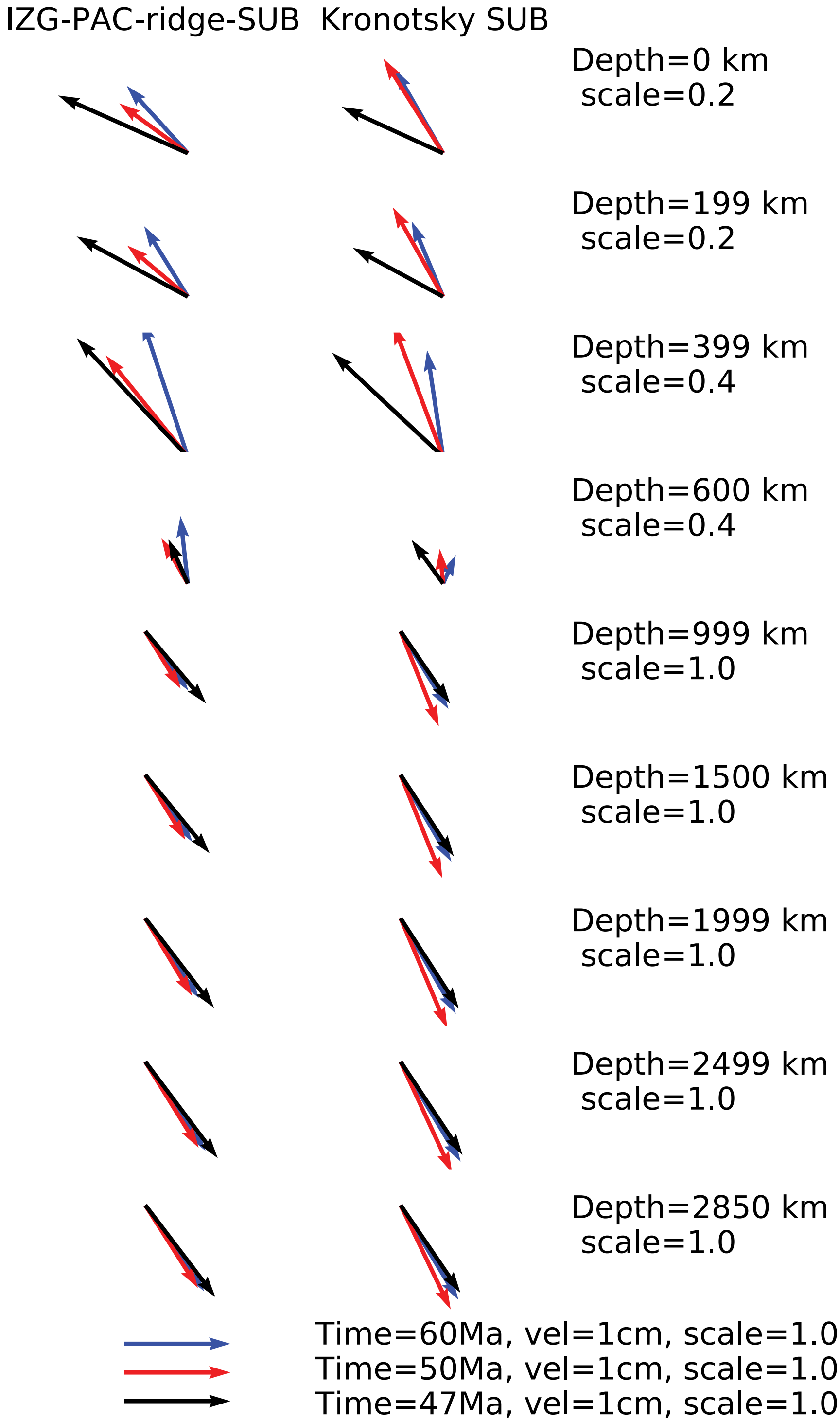

Extended Data Fig. 9 | Geodynamically predicted horizontal velocity in the vicinity of Hawaiian plume as a function of depth for different models. Geodynamically predicted horizontal velocity in the vicinity of Hawaiian plume as a function of depth for different models. For each depth, the velocities are averaged over the region from 190°E to 220°E and from 10°N to 35°N. The blue arrows represent the averaged velocities at 60 Ma, the red arrows at 50 Ma and the black arrows at 47 Ma.